


Lagrangian properties of the entrainment across turbulent/non-turbulent interface layers

Cite as: Phys. Fluids **28**, 031701 (2016); <https://doi.org/10.1063/1.4942959>

Submitted: 14 July 2015 • Accepted: 16 February 2016 • Published Online: 02 March 2016

Tomoaki Watanabe,  Carlos B. da Silva,  Yasuhiko Sakai, et al.



View Online



Export Citation



CrossMark

ARTICLES YOU MAY BE INTERESTED IN

[Turbulent mixing of passive scalar near turbulent and non-turbulent interface in mixing layers](#)

Physics of Fluids **27**, 085109 (2015); <https://doi.org/10.1063/1.4928199>

[Turbulent/non-turbulent interfaces detected in DNS of incompressible turbulent boundary layers](#)

Physics of Fluids **30**, 035102 (2018); <https://doi.org/10.1063/1.5022423>

[Enstrophy and passive scalar transport near the turbulent/non-turbulent interface in a turbulent planar jet flow](#)

Physics of Fluids **26**, 105103 (2014); <https://doi.org/10.1063/1.4898208>

APL Machine Learning

Open, quality research for the networking communities

Now Open for Submissions

LEARN MORE

Lagrangian properties of the entrainment across turbulent/non-turbulent interface layers

Tomoaki Watanabe,^{1,2,a)} Carlos B. da Silva,² Yasuhiko Sakai,³ Koji Nagata,¹ and Toshiyuki Hayase⁴

¹*Department of Aerospace Engineering, Nagoya University, Nagoya, Japan*

²*LAETA, IDMEC, Instituto Superior Técnico, Universidade de Lisboa, Lisboa, Portugal*

³*Department of Mechanical Science and Engineering, Nagoya University, Nagoya, Japan*

⁴*Institute of Fluid Science, Tohoku University, Sendai, Japan*

(Received 14 July 2015; accepted 16 February 2016; published online 2 March 2016)

Lagrangian statistics obtained from direct numerical simulations of turbulent planar jets and mixing layers are reported for the separation distance between the tracer particles at the outer edge of the turbulent/non-turbulent interface layer, and the entrained fluid particles. In the viscous superlayer (VSL) the mean square particle distance exhibits a ballistic evolution, while the Richardson-like scaling for relative dispersion prevails inside the turbulent sublayer (TSL). The results further support the existence of two different regimes within the interface layer, where small-scale outward enstrophy diffusion governs the entrained particles in the VSL, while inviscid small-scale motions govern the TSL. © 2016 AIP Publishing LLC. [<http://dx.doi.org/10.1063/1.4942959>]

The evolution of turbulent flows surrounded by laminar flow regions is an ubiquitous phenomenon of fundamental importance for various flows found in engineering and the environment, such as in chemical reactors,¹ and turbulent patches in the ocean and atmosphere.² It is also found in canonical flows, such as jets, mixing layers, and boundary layers, where turbulence development occurs together with the entrainment of irrotational fluid, which is deeply linked to the transport and mixing within the fluid, in an interplay with important consequences for the turbulence dynamics.³

Turbulent entrainment has been recently studied in relation to the interfacial layer which separates turbulent from irrotational (non-turbulent) flow: the so-called turbulent/non-turbulent interface (TNTI).^{4,5} The long-standing question of turbulent entrainment has been the understanding of what are the physical mechanisms causing it. Turbulent motions with wide range of scales have been observed near TNTIs, from small-scale eddies, which are statistically universal, to large-scale structures, which are flow dependent, while both small and large-scale motions are expected to contribute to the turbulent entrainment by nibbling and engulfment, respectively.⁶ As the turbulent entrainment takes place, irrotational fluid crosses the TNTI due to some mechanism. The TNTI is often detected using a constant vorticity magnitude isosurface,⁶ and for this reason turbulent entrainment has been investigated by analyzing this isosurface propagation, whose velocity is of the order of the Kolmogorov velocity $v_\eta \equiv (\nu\varepsilon)^{1/4}$, reflecting the importance of small-scale features,⁵ where ε is the dissipation rate of turbulent kinetic energy and ν is the kinematic viscosity. However, recent studies on the structure of TNTI showed that it displays a finite thickness,⁷ consisting of two layers: the viscous superlayer (VSL) and the turbulent sublayer (TSL).⁶ Thus, entrainment can be more precisely described as the irrotational fluid movements across this layer rather than the fluid moving through an infinitely thin surface.

The Lagrangian approach to turbulent flows is particularly useful for this purpose and it has been used for investigating the turbulent characteristics before and after fluid particles (tracers) cross the surface representing the outer edge of the TNTI.^{8–10} Because the TNTI location fluctuates,

a) watanabe.tomoaki@c.nagoya-u.jp

the Lagrangian tracking of fluid particles within the TNTI layer is crucial to better understand turbulent entrainment since the vorticity dynamics is quite different within the VSL and TSL.⁷

In this letter, we report the entrainment characteristics across the entire TNTI layer obtained using a Lagrangian approach, where the location of the entrained fluid particles within the TNTI layer is examined by tracking the outer edge of the TNTI, which is defined as an infinitely thin surface referred to as the *irrotational boundary* hereafter. With this definition, the VSL is located just inside the irrotational boundary, while the TSL appears between the VSL and the turbulent core region.⁶ The results show that the statistical properties of the entrained particle movements can be explained solely by small-scale turbulence features.

Direct numerical simulations (DNSs) are performed for temporally developing mixing layers¹¹ and planar jets,⁷ which are periodic in the streamwise (x) and spanwise (z) directions and spread in the cross-streamwise (y) direction, where the slip boundary conditions are applied at the lateral boundaries. The same boundary conditions were used in the recent DNS of temporally evolving free shear flows.¹² In this study, new simulations are performed for investigating the Lagrangian properties of turbulent entrainment. The origin of the coordinate system is located at the center of the computational domain, which has a size of $L_x \times L_y \times L_z$ and is represented by $N_x \times N_y \times N_z$ grid points. The DNS code is an incompressible Navier–Stokes solver based on the fractional step method, finite differences for spatial discretization, and the 3rd-order Runge–Kutta method for temporal advancement and was used in previous studies.¹¹ The 4th-order and 2nd-order fully conservative central difference schemes are used in the periodic and cross-streamwise directions, respectively. The initial velocity fields consist of statistically homogeneous and isotropic velocity fluctuations generated by a diffusion process as in our previous paper¹¹ and the mean streamwise velocity is given by $0.5U_M \tanh(2y/\theta_M)$ in the mixing layers and $0.5U_J + 0.5U_J \tanh[(H - 2|y|)/4\theta_J]$ in the planar jets. Here, U_M is the velocity difference in the mixing layers, U_J the jet velocity, H the width of the jet inlet, and θ_M (θ_J) the initial shear layer thickness in the mixing layers (planar jets). We set $\theta_J = 0.015H$, and the other parameters are determined via the Reynolds numbers Re defined by $U_M\theta_M/\nu$ and U_JH/ν . The grid is equidistant in the x and z directions while a fine grid is used near $y = 0$ in the y direction. The physical and computational parameters are listed in Table I.

Lagrangian statistics of the fluid particles during the turbulent entrainment process are obtained using a similar method as described in a previous study.⁹ Once the DNS of mixing layers and planar jets have reached a self-similar state, 140 000 fluid particles are randomly seeded in the non-turbulent region close to the irrotational boundary detected as an isosurface of small vorticity magnitude $|\omega| = \omega_{th}$, whose value is determined by using the dependence of the turbulent volume on ω_{th} .⁹ This isosurface corresponds to the enstrophy isosurface $\omega^2/2 = \omega_{th}^2/2$. Here, the region of $|\omega|$ larger (smaller) than ω_{th} is referred to as a turbulent (non-turbulent) region. The fluid particles are introduced at time $t_0 = 130\theta_M/U_M$ and $32H/U_J$ in the DNS of mixing layers and planar

TABLE I. Physical and computational parameters of the DNS. The displayed turbulence characteristics are from the turbulent core regions.

Run	ML04	ML08	PJ50	PJ90
Flow type	Mixing layer	Mixing layer	Planar jet	Planar jet
Re	400	800	5000	9000
L_x	$16\pi\theta_M$	$16\pi\theta_M$	$2.4\pi H$	$2.6\pi H$
L_y	$16\pi\theta_M$	$16\pi\theta_M$	$4.8\pi H$	$3.8\pi H$
L_z	$8\pi\theta_M$	$8\pi\theta_M$	$2.4\pi H$	$1.3\pi H$
N_x, N_y, N_z	512, 500, 256	1024, 700, 512	512, 850, 512	1024, 1150, 512
Time step dt	$0.08\theta_M/U_M$	$0.04\theta_M/U_M$	$0.012H/U_J$	$0.006H/U_J$
$\Delta_x = \Delta_z, \Delta_y$ at $y = 0$	$1.5\eta, 1.0\eta$	$1.2\eta, 1.1\eta$	$1.5\eta, 1.2\eta$	$1.4\eta, 1.2\eta$
Re_λ	105	151	94	158
η	$0.064\theta_M$	$0.041\theta_M$	$0.0096H$	$0.0059H$
λ	20.8η	23.3η	14.8η	20.3η
$\langle v_E \rangle$	$0.47v_\eta$	$0.39v_\eta$	$0.43v_\eta$	$0.41v_\eta$

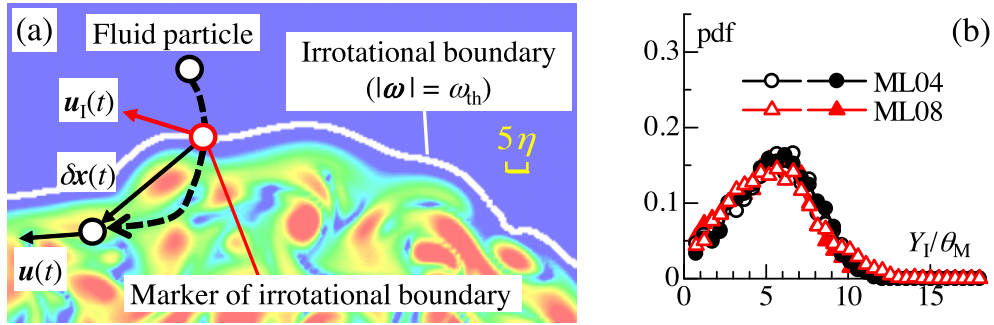


FIG. 1. (a) The fluid particle movement is analyzed in relation to the irrotational boundary, which is tracked by using a marker introduced on the boundary where the fluid particle crosses it. The irrotational boundary is indicated in the figure by a thick white line. The color contours show enstrophy levels in $\log_{10}(\omega^2/2)$ for simulation ML08. (b) Pdfs of the irrotational boundary height (Y_I) from $y = 0$ in mixing layers obtained from isosurface of vorticity magnitude (lines with open symbols) and markers of irrotational boundary (lines with closed symbols).

jets, respectively, and the turbulence characteristics in the turbulent core region, such as the Kolmogorov lengthscale $\eta \equiv (\nu^3/\varepsilon)^{1/4}$, Taylor microscale λ calculated from the streamwise velocity, and turbulent Reynolds number $\text{Re}_\lambda = u_{\text{rms}}\lambda/\nu$, at $t = t_0$ are summarized in Table I, where u_{rms} is the rms streamwise velocity fluctuation.

The fluid particles are tracked using a 3rd-order Runge–Kutta scheme for temporal advancement and a tri-linear interpolation scheme as in Yang *et al.*¹³ In addition to the fluid particles, the irrotational boundary defined by a constant enstrophy isosurface is also tracked by the following method. When a fluid particle in the non-turbulent region crosses the irrotational boundary, a marker is introduced at this point (Fig. 1(a)). Subsequently, the marker is also tracked using the velocity of the irrotational boundary $\mathbf{u}_I = \mathbf{u}_0 + \mathbf{u}_P$, which is the sum of the fluid velocity \mathbf{u}_0 and the propagation velocity of the irrotational boundary $\mathbf{u}_P = v_E \mathbf{n}$,⁵ where $\mathbf{n} = -\nabla\omega^2/|\nabla\omega^2|$ is the unit normal vector of the irrotational boundary, and $v_E = (2\omega_i S_{ij}\omega_j + 2\nu\omega_i \nabla^2\omega_i)/|\nabla\omega^2|$ (ω_i is the vorticity and S_{ij} is the rate-of-strain tensor).⁵ The mean propagation velocity $\langle v_E \rangle$ at $t = t_0$ is shown in Table I. This marker represents the location of the isosurface of $|\omega| = \omega_{\text{th}}$ ($\omega^2/2 = \omega_{\text{th}}^2/2$). Previous studies have shown that only a negligible fraction of particles ends up trapped inside a non-turbulent region completely surrounded by turbulent fluids (irrotational 3D bubbles).⁹ The irrotational boundary of this region disappears after it becomes turbulent. Therefore, the markers of these irrotational boundaries are no longer located on isosurfaces of $|\omega| = \omega_{\text{th}}$. For precluding these events, $|\omega|$ on the markers is monitored at every time step, while markers with $|\omega| > 2\omega_{\text{th}}$ are not used in the subsequent analysis. Note that this work focuses on the entrained fluid particle movements across the TNTI layer, rather than on the movement of non-turbulent fluid packets. Figure 1(b) shows the probability density function (pdf) of the irrotational boundary height in the mixing layers, where the pdfs are calculated from isosurfaces of constant $|\omega| = \omega_{\text{th}}$ and the locations of the markers, both yielding similar results, which validates the boundary tracking algorithm.

Lagrangian conditional statistics were calculated for the fluid particles, conditioned on the time τ elapsed after a fluid particle has crossed the irrotational boundary. We also use Eulerian statistics conditioned on the distance y_I from the irrotational boundary as in previous studies.¹¹ The y_I direction is given by \mathbf{n} , and the turbulent region is represented by $y_I < 0$. Hereafter, the Lagrangian and Eulerian conditional averages are denoted by $\langle * \rangle_\tau$ and $\langle * \rangle_{y_I}$, respectively, while the fluid particle location relative to the irrotational boundary is represented by a separation vector $\delta\mathbf{x}(\tau)$ in Fig. 1(a). The irrotational boundary movement cannot be neglected because of the convection. $\delta\mathbf{x}$ is introduced for examining the particle location within the TNTI layer. As we discuss below, $\delta\mathbf{x}$ aligns with the normal of the irrotational boundary, \mathbf{n} , for small τ , enabling us to relate the particle location to the VSL and TSL.

Figure 2(a) shows the Lagrangian conditional average of $\delta x \equiv |\delta\mathbf{x}|$, where $\delta\mathbf{x}$ and τ are normalized by the Kolmogorov lengthscale η and time scale $\tau_\eta \equiv (\nu/\varepsilon)^{1/2}$ at $t = t_0$. The mean thickness of the VSL, δ_ν , is estimated from the Eulerian conditional enstrophy budget within the TNTI, as

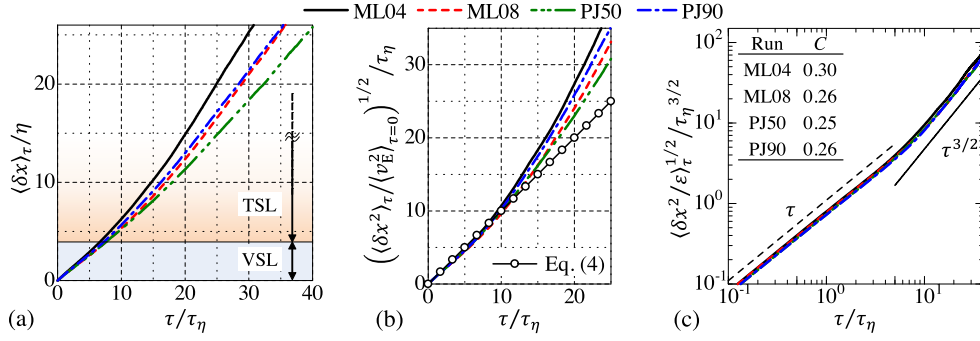


FIG. 2. (a) Lagrangian conditional average of the distance between fluid particles position and the irrotational boundary marker. The VSL and TSL estimated from their mean thicknesses in simulation ML08 are highlighted. (b) Lagrangian conditional root-mean-squared distance divided by the root-mean-squared propagation velocity. (c) Lagrangian conditional root-mean-squared distance between the fluid particles position and the irrotational boundary marker, normalized by ε at $y = 0$. The thin solid and dashed lines indicate the power laws $\langle \delta x^2 \rangle_\tau^{1/2} \propto \tau^{3/2}$ and $\propto \tau$, respectively. The constant C defined in Eq. (5) and shown in the figure has been estimated using the least-squares method.

the length of the region where the enstrophy production $\langle \omega_i S_{ij} \omega_j \rangle_{yI}$ is smaller than the viscous diffusion $\langle \nu \nabla^2 (\omega^2/2) \rangle_{yI}$ as in Ref. 7. Then, the mean thickness of the TSL, δ_ω , is estimated as the distance between the VSL and the location at which $\langle \omega^2/2 \rangle_{yI}$ reaches the same value inside the turbulent core region. We obtained $\delta_\nu \approx 4\eta$, and $\delta_\omega = 9\eta \sim 11\eta$. The present values of δ_ν and δ_ω agree with Refs. 7 and 12. Figure 2(a) shows that it takes about $7\tau_\eta$ for the fluid particles to move across the VSL and to reach the TSL for all simulations. However, the different configurations and Reynolds number naturally affect the time needed for the particles to move across the TSL. Note that the boundary between the TSL and the turbulent core region is not clear in Fig. 2(a) because deep inside the TSL the entrained particles are not anymore in the boundary normal direction (see Fig. 3(a)).

A fluid particle location relative to a marker of the irrotational boundary, $\delta \mathbf{x}(\tau)$, changes as

$$\frac{d\delta \mathbf{x}(\tau)}{d\tau} = \delta \mathbf{u}(\tau) \equiv \mathbf{u}(\tau) - \mathbf{u}_I(\tau), \quad (1)$$

where $\delta \mathbf{u}$ is the velocity of the fluid particle relative to the velocity of the marker of the irrotational boundary, and is simply referred to as the relative velocity. Taking the dot-product of Eq. (1) with $\delta \mathbf{x}$ we obtain the following equation:¹⁴

$$\frac{d\delta x^2}{d\tau} = 2 \int_0^\tau \delta \mathbf{u}(\tau) \cdot \delta \mathbf{u}(\tau') d\tau'. \quad (2)$$

The relative velocity is represented by $\delta \mathbf{u}(\tau) = (\mathbf{u}(\tau) - \mathbf{u}_0(\tau)) - \mathbf{u}_p(\tau)$, where $(\mathbf{u}(\tau) - \mathbf{u}_0(\tau))$ is the fluid velocity difference between the fluid particle and the location of the marker of the irrotational

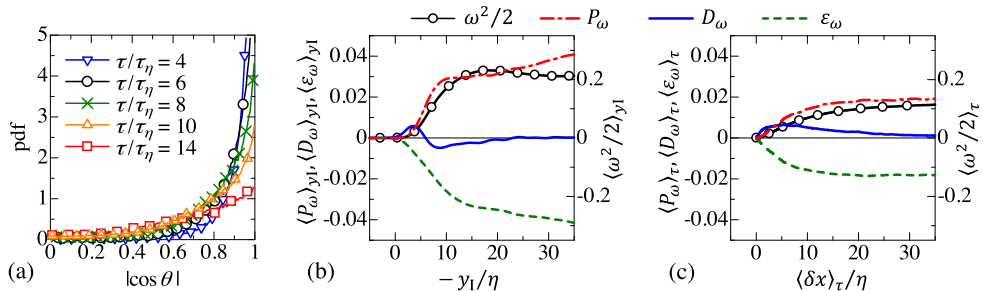


FIG. 3. (a) Conditional pdf of the cosine of the angle between the separation vector $\delta \mathbf{x}$ and the irrotational boundary normal \mathbf{n} in the simulation ML08. (b) Eulerian and (c) Lagrangian conditional averages of enstrophy ($\omega^2/2$) and enstrophy budget in simulation ML08 (production: $P_\omega = \omega_i S_{ij} \omega_j$, viscous diffusion: $D_\omega = \nu \nabla^2 (\omega^2/2)$, and dissipation: $\varepsilon_\omega = -\nu \nabla \omega_i \cdot \nabla \omega_i$). The results are normalized by U_M and θ_M . The Lagrangian statistics are plotted against $\langle \delta x \rangle_\tau / \eta$ for $\tau \geq 0$.

boundary. For small τ , fluid particles are located very close to the irrotational boundary, and the relative velocity can be approximated by $\delta \mathbf{u}(\tau) \approx -\mathbf{u}_p(0)$.¹⁵ Thus, Eq. (2) is simply,

$$\frac{d\delta x^2}{d\tau} = 2 \int_0^\tau (\mathbf{u}_p(0) \cdot \mathbf{u}_p(0)) dt' = 2v_E^2 \tau. \quad (3)$$

Integrating Eq. (3) yields $\delta x^2 = v_E^2 \tau^2$, where v_E is taken at $\tau = 0$. Thus, the Lagrangian conditional root-mean-squared distance changes according to

$$\langle \delta x^2 \rangle_\tau^{1/2} = \langle v_E^2 \rangle_{\tau=0}^{1/2} \tau \quad (\text{for small } \tau). \quad (4)$$

Figure 2(b) gives $\langle \delta x^2 \rangle_\tau^{1/2}$ showing that the DNS results follow Eq. (4) for $\tau/\tau_\eta \lesssim 10$. Thus, within the VSL, δx is determined by the irrotational boundary propagation velocity, whose direction is given by the boundary normal. Therefore, the fluid particles reach the TSL because of the outward enstrophy diffusion, which results in the propagation of the irrotational boundary, and the particles inside the VSL stay in the direction normal to the irrotational boundary.

When a fluid particle is located far away from the irrotational boundary, the fluid velocity difference is expected to be large compared with the propagation velocity ($\delta \mathbf{u} \approx \mathbf{u} - \mathbf{u}_0$).¹⁵ Therefore, the problem is similar to two-particles dispersion.¹⁶ Similarly to Richardson's law for the relative diffusion, under the assumption that only eddies of size $\delta x(\tau)$ contribute to the change in δx ,¹⁷ we can obtain the following relationship for the self-similar regions:¹⁸

$$\langle \delta x^2 / \varepsilon \rangle_\tau^{1/2} = C \tau^{3/2} \quad (\text{for large } \tau), \quad (5)$$

where C is a constant and ε is obtained in the turbulent core region.

Figure 2(c) shows $\langle \delta x^2 / \varepsilon \rangle_\tau^{1/2}$ against τ . For $\tau \approx 0$, Eq. (4) suggests $\langle \delta x^2 / \varepsilon \rangle_\tau^{1/2} \propto \tau$. It is found that $\langle \delta x^2 / \varepsilon \rangle_\tau^{1/2}$ is qualitatively independent of flow configurations and of the Reynolds number, and the scaling laws of Eqs. (4) and (5) are recovered in all simulations. Interestingly, $\langle \delta x^2 / \varepsilon \rangle_\tau^{1/2}$ begins to obey Eq. (5) from $\tau/\tau_\eta \approx 9$ slightly after the particles move into the TSL (Fig. 2(a)), and it holds even for larger τ/τ_η . The values of the constant C in Eq. (5) displayed in Fig. 2(c) have been obtained in the present DNSs with the least-squares methods and oscillate between 0.25 and 0.30. Here, we recall again that the relationship $\langle \delta x^2 / \varepsilon \rangle_\tau^{1/2} \sim \tau^{3/2}$ is obtained under the assumption that the fluid particle movement within the TNTI layer is caused solely by eddies of size δx , independently of viscous effects, and of much larger or much smaller eddy sizes and is valid for the entrained particles within the TSL, $\delta_\nu \lesssim \delta x \lesssim \delta_\nu + \delta_\omega$. This indicates that the entrainment across the TSL is caused by the small-scale eddies with these eddy sizes, rather than by viscous effects and larger-scale structures, which can cause fluid engulfment within the TNTI.¹⁹ Indeed, eddies with core radius of about 5η ($\approx \delta_\nu$) were observed within the TSL.²⁰

Figure 3(a) shows the pdf of the cosine of the angle between $\delta \mathbf{x}$ and \mathbf{n} , which has a large peak associated with a parallel alignment of these vectors. Thus, for small τ the particles are located in the irrotational boundary normal direction as expected from Eq. (4). Figures 3(a) and 3(b) compare the Eulerian and Lagrangian conditional statistics of the enstrophy and enstrophy budget in simulation ML08 (the Lagrangian statistics are plotted against $\langle \delta x \rangle_\tau$). Qualitative differences arise in the Eulerian and Lagrangian conditional means of D_ω . The Eulerian $\langle D_\omega \rangle_{y1}$ displays both positive and negative values, indicating a mean enstrophy transport from the turbulent region into the irrotational region, while $\langle D_\omega \rangle_\tau$ is always positive even for large $\langle \delta x \rangle_\tau$. Thus, even after the entrained fluid has acquired an important level of enstrophy, D_ω has no mean contribution to the enstrophy transport towards the non-turbulent region, associated with the outward propagation of the irrotational boundary. Wolf *et al.* showed that the Lagrangian conditional mean enstrophy is smaller than the Eulerian counterpart for $\tau/\tau_\eta \leq 8$. The same tendency can be observed here (e.g., Fig. 3) even for much larger τ/τ_η . The Lagrangian enstrophy production and dissipation terms observed here are also smaller than their corresponding Eulerian counterparts, owing to a smaller enstrophy level in the Lagrangian statistics.

Figure 4(a) shows the Eulerian and Lagrangian conditional averages of the second invariant of velocity gradient tensor $Q = (\omega_i \omega_i - 2S_{ij}S_{ij})/4$, where the trajectories of the entrained fluid particles are related to the small-scale turbulence structures since its large positive value implies the

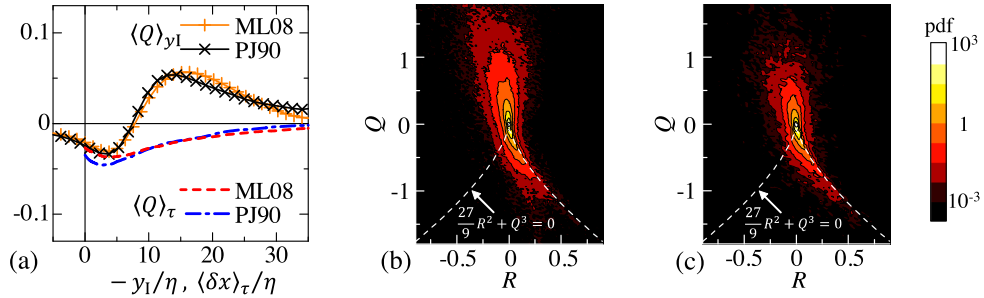


FIG. 4. (a) Eulerian and Lagrangian conditional averages of Q , where again the Lagrangian statistics are plotted against $\langle \delta x \rangle_\tau$. Eulerian (b) and Lagrangian (c) conditional joint pdfs of Q and R in ML08. The joint pdfs are calculated at $y_1/\eta = -9$ in (b) and $\tau/\tau_\eta = 16$ in (c), at which $\langle \delta x \rangle_\tau / \eta = 9$. In all figures, the invariants and pdfs are normalized by the mean strain product in the turbulent core region.

predominance of vorticity over the strain, as in the vortex core region of an eddy,¹⁷ while $Q < 0$ tends to appear outside the vortex core region, where dissipation is dominant. $\langle Q \rangle_{y1}$ has a negative peak near the irrotational boundary and a large positive peak inside the turbulent region while $\langle Q \rangle_\tau$ is negative and tends to $\langle Q \rangle_\tau = 0$ in the turbulent core region. Figures 4(b) and 4(c) compare the conditional joint pdf of Q and $R = -(S_{ij}S_{jk}S_{ki}/3 - \omega_i S_{ij} \omega_j/4)$ (the third invariant of the velocity gradient tensor) in the TSL obtained as the Eulerian and Lagrangian statistics. Both pdfs show a “teardrop” shape similar to various turbulent flows, but a difference is found for large positive Q . Specifically the probability of finding intense values of $Q \gg 0$ is much smaller in the Lagrangian than in the Eulerian pdfs. Thus, although within the TNTI layer there is a region where $Q \gg 0$, as the fluid particles are entrained they tend to circumvent these regions moving across regions with relatively small Q . This may be explained by a circular motion induced by the intense eddies existing within the TNTI layer, which makes the fluid particles move around the eddies where stronger values of Q are to be found. Within the VSL the Eulerian and Lagrangian conditional averages are similar, and the contribution from turbulent fluid packets in the turbulent core region is expected to be small for the Eulerian statistics. This agrees with recent results from high-Schmidt number scalar statistics showing that the VSL mostly consists of entrained fluid from the non-turbulent region.¹¹

In summary, Lagrangian statistics taken during the entrainment of fluid particles across the TNTI layer confirm that the entrainment is caused by the two distinct physical processes depending on the location within the TNTI layer, i.e., viscous effects within the VSL and inertial effects linked to the small-scale eddies within the TSL. The entrained fluid particles penetrate into the TSL by the propagation of the outer edge of the TNTI, which takes place owing to the outward viscous diffusion of enstrophy. Moreover, the invariants of the velocity gradient tensor show the connection between the entrainment process and the small-scale eddy structures, suggesting that the entraining fluid particles move around the vortex cores of the small-scale eddies near the TNTI layer. Finally, it is shown that the Lagrangian statistics are governed solely by small-scale turbulence characteristics and that large-scale effects, resulting from different flow configurations, cannot be observed, which opens the possibility for a unified entrainment model solely based on the small-scale eddy characteristics.

Part of this work was conducted under the Collaborative Research Project of the Institute of Fluid Science, Tohoku University. This work was supported by JSPS KAKENHI Grant No. 25002531 and MEXT KAKENHI Grant Nos. 25289030 and 25289031. This work has been supported by Fundação para a Ciência e a Tecnologia (FCT), through IDMEC, under LAETA, projects PTDC/EME-MFE/122849/2010 and UID/EMS/50022/2013.

¹ J. C. Hill, “Homogeneous turbulent mixing with chemical reaction,” *Annu. Rev. Fluid Mech.* **8**, 135 (1976).

² J. J. Riley and M. P. Lelong, “Fluid motions in the presence of strong stable stratification,” *Annu. Rev. Fluid Mech.* **32**, 613 (2000).

³ P. E. Dimotakis, “Turbulent mixing,” *Annu. Rev. Fluid Mech.* **37**, 329 (2005).

- ⁴ J. Westerweel, C. Fukushima, J. M. Pedersen, and J. C. R. Hunt, "Mechanics of the turbulent-nonturbulent interface of a jet," *Phys. Rev. Lett.* **95**, 174501 (2005).
- ⁵ M. Holzner and B. Lüthi, "Laminar superlayer at the turbulence boundary," *Phys. Rev. Lett.* **106**, 134503 (2011).
- ⁶ C. B. da Silva, J. C. R. Hunt, I. Eames, and J. Westerweel, "Interfacial layers between regions of different turbulence intensity," *Annu. Rev. Fluid Mech.* **46**, 567 (2014).
- ⁷ R. R. Taveira and C. B. da Silva, "Characteristics of the viscous superlayer in shear free turbulence and in planar turbulent jets," *Phys. Fluids* **26**, 021702 (2014).
- ⁸ M. Holzner, A. Liberzon, N. Nikitin, B. Lüthi, W. Kinzelbach, and A. Tsinober, "A Lagrangian investigation of the small-scale features of turbulent entrainment through particle tracking and direct numerical simulation," *J. Fluid Mech.* **598**, 465 (2008).
- ⁹ R. R. Taveira, J. S. Diogo, D. C. Lopes, and C. B. da Silva, "Lagrangian statistics across the turbulent-nonturbulent interface in a turbulent plane jet," *Phys. Rev. E* **88**, 043001 (2013).
- ¹⁰ M. Wolf, M. Holzner, B. Lüthi, D. Krug, W. Kinzelbach, and A. Tsinober, "Effects of mean shear on the local turbulent entrainment process," *J. Fluid Mech.* **731**, 95 (2013).
- ¹¹ T. Watanabe, Y. Sakai, K. Nagata, Y. Ito, and T. Hayase, "Turbulent mixing of passive scalar near turbulent and non-turbulent interface in mixing layers," *Phys. Fluids* **27**, 085109 (2015).
- ¹² M. van Reeuwijk and M. Holzner, "The turbulence boundary of a temporal jet," *J. Fluid Mech.* **739**, 254 (2014).
- ¹³ Y. Yang, J. Wang, Y. Shi, Z. Xiao, X. T. He, and S. Chen, "Acceleration of passive tracers in compressible turbulent flow," *Phys. Rev. Lett.* **110**, 064503 (2013).
- ¹⁴ G. K. Batchelor, "The application of the similarity theory of turbulence to atmospheric diffusion," *Q. J. R. Meteorol. Soc.* **76**, 133 (1950).
- ¹⁵ T. Watanabe, Y. Sakai, K. Nagata, Y. Ito, and T. Hayase, "Vortex stretching and compression near the turbulent/nonturbulent interface in a planar jet," *J. Fluid Mech.* **758**, 754 (2014).
- ¹⁶ J. P. L. C. Salazar and L. R. Collins, "Two-particle dispersion in isotropic turbulent flows," *Annu. Rev. Fluid Mech.* **41**, 405 (2009).
- ¹⁷ P. A. Davidson, *Turbulence: An Introduction for Scientists and Engineers* (Oxford University Press, 2004).
- ¹⁸ M. Larcheveque and M. Lesieur, "The application of eddy-damped Markovian closures to the problem of dispersion of particle pairs," *J. Méc.* **20**, 113 (1981).
- ¹⁹ J. C. R. Hunt, I. Eames, and J. Westerweel, "Vortical interactions with interfacial shear layers," in *Proceedings of IUTAM Symposium on Computational Physics and New Perspectives in Turbulence, Nagoya, 2006*, edited by Y. Kaneda (Springer, 2008), pp. 331–338.
- ²⁰ C. B. da Silva, R. J. N. dos Reis, and J. C. F. Pereira, "The intense vorticity structures near the turbulent/non-turbulent interface in a jet," *J. Fluid Mech.* **685**, 165 (2011).